APPLIED PHYSICS

Asymmetric hot-carrier thermalization and broadband photoresponse in graphene-2D semiconductor lateral heterojunctions

Yuxuan Lin[1]*, Qiong Ma[2]*, Pin-Chun Shen[1]*, Batyr Ilyas[2], Yaqing Bie[2], Albert Liao[1], Emre Ergeçen[2], Bingnan Han[1,3], Nannan Mao[1], Xu Zhang[1], Xiang Ji[1], Yuhao Zhang[1], Jihao Yin[3], Shengxi Huang[4], Mildred Dresselhaus[1,2†], Nuh Gedik[2], Pablo Jarillo-Herrero[2], Xi Ling[5‡], Jing Kong[1‡], Tomás Palacios[1‡]

The massless Dirac electron transport in graphene has led to a variety of unique light-matter interaction phenomena, which promise many novel optoelectronic applications. Most of the effects are only accessible by breaking the spatial symmetry, through introducing edges, p-n junctions, or heterogeneous interfaces. The recent development of direct synthesis of lateral heterostructures offers new opportunities to achieve the desired asymmetry. As a proof of concept, we study the photothermoelectric effect in an asymmetric lateral heterojunction between the Dirac semimetallic monolayer graphene and the parabolic semiconducting monolayer MoS_2. Very different hot-carrier cooling mechanisms on the graphene and the MoS_2 sides allow us to resolve the asymmetric thermalization pathways of photoinduced hot carriers spatially with electrostatic gate tunability. We also demonstrate the potential of graphene-2D semiconductor lateral heterojunctions as broadband infrared photodetectors. The proposed structure shows an extreme in-plane asymmetry and provides a new platform to study light-matter interactions in low-dimensional systems.

INTRODUCTION

Breaking spatial symmetry in materials like graphene is a powerful tool to enhance or even induce new forms of light-matter interactions (*1*). For instance, edges and grain boundaries in graphene samples have been used to control surface plasmons (*2*–*4*). At the same time, electrostatic-gated homojunctions enable the hot carrier–mediated photothermoelectric (PTE) effect in graphene (*5*–*8*). An additional degree of freedom is given by vertical heterostructure assembly (*9*) of two-dimensional (2D) materials through aligned layer-by-layer stacking. This has made it possible not only to leverage the asymmetry in the out-of-plane direction but also to design artificial lattices with engineered symmetry through twisted angles between the layers (*10*–*12*). All of these have allowed the recent discovery of many previously unidentified light-matter interaction phenomena on 2D vertical heterostructures, including interlayer excitonics/valleytronics (*13*, *14*), photoexcited thermionic emission/tunneling (*15*, *16*), fluorescence intermittency (*17*), and tunable twisted-angle circular dichroism (*18*). In parallel, several groups have developed synthetic methods for lateral heterostructures with precise spatial confinement through either selective seeding or epitaxy, which further extended the design space for multifunctional and high-performance electronic and optoelectronic devices and systems based on 2D heterostructures (*19*–*29*). One good example is the tunable photoluminescence (PL) emissions induced by the epitaxial strain in WS_2-WSe_2 coherent superlattices (*29*). In spite of all this remarkable progress, the light-matter interactions of highly asymmetric lateral heterojunctions such as those between graphene and 2D semiconductors have not been explored.

Here, we aim to study the photoelectric response at graphene-2D semiconductor lateral heterojunctions. The massless Dirac transport in graphene leads to a unique hot-electron PTE effect (*5*–*8*, *30*). Because of the ultrafast electron-electron scatterings (on the order of 10 fs) (*31*, *32*) and relatively slow electron-phonon scatterings (on the order of picoseconds) (*33*–*37*), the photoinduced carriers are thermalized by the electronic system and dissipate the heat very slowly to the lattice. In a conventional semiconductor with parabolic electronic dispersion, on the other hand, the photoinduced electrons and holes either are separated and collected directly by a built-in electric field [the photovoltaic (PV) effect] or scatter strongly with phonons and impurities and transfer their kinetic energy to heat or lattice vibrations. If the Dirac semimetallic graphene and the parabolic 2D semiconductor are put in close proximity with each other within the 2D plane, then the vast asymmetry of the energy transfer pathways on the two sides gives rise to very interesting features that can be addressed spatially through localized light excitation. In this work, we demonstrate such asymmetric hot-electron thermalization on a synthetic graphene-MoS_2 lateral heterojunction. From gate-dependent scanning photocurrent measurement, we were able to confirm that the PTE effect dominates the photoresponse at the lateral junction when the excitation photon energy is below the MoS_2 bandgap. A theoretical model was built to understand the asymmetric thermalization pathways of the photoinduced hot carriers at the junction, which matched our experimental observations very well. Spectral photoresponse measurements also suggested that the graphene-MoS_2 lateral heterojunction could potentially be used as a broadband infrared detector. Our proposed asymmetric lateral heterostructure provides a new platform to study novel light-matter interactions in

[1]Department of Electrical Engineering and Computer Science, Massachusetts Institute of Technology, Cambridge, MA 02139, USA. [2]Department of Physics, Massachusetts Institute of Technology, Cambridge, MA 02139, USA. [3]School of Astronautics, Beihang University, Beijing 100191, China. [4]Department of Electrical Engineering, The Pennsylvania State University, University Park, PA 16802, USA. [5]Department of Chemistry and Division of Materials Science and Engineering, Boston University, Boston, MA 02215, USA.
*These authors contributed equally to this work.
†Deceased.
‡Corresponding author. Email: xiling@bu.edu (X.L.); jingkong@mit.edu (J.K.); tpalacios@mit.edu (T.P.)

2D materials, especially for those that can be enhanced by spatial symmetry breaking, such as photoelectric and plasmonic effects in graphene and exciton transports in 2D semiconductors.

RESULTS AND DISCUSSION

Figure 1A shows a schematic of the lateral graphene-MoS_2 heterojunction device. The graphene-MoS_2 lateral heterostructures were obtained through the seeding promoter–assisted chemical vapor deposition (CVD) that we developed previously (see Materials and Methods for details) (*25*, *38*). Atomic force microscopic (AFM) images, high-resolution transmission electron microscopic (HRTEM) images, and Raman and PL mappings (figs. S1 to S3) at the graphene-MoS_2 interfaces confirm that the two materials overlap only a few tens of nanometers at the interface (*25*). Note that such a nanometer-scale overlap does not substantially affect the photoresponse at the interfaces because the optical excitations cannot resolve any structural features that are below the wavelengths, and both the depletion width (on the order of 100 nm) (*39*) in a PV effect and the cooling length (on the order of 100 nm to 1 μm) (*5*, *7*, *36*) in a PTE effect are sufficiently larger than the size of the overlaps. Figure 1B shows the optical microscopic image of the graphene-MoS_2 lateral heterojunction device. We fabricated multiple long and short electrodes near the graphene-MoS_2 interface to perform transport and photocurrent measurement on both the lateral junction and each homogeneous material. All the devices were fabricated on top of a 285-nm SiO_2/Si wafer, and the Si substrate served as a back gate. Figure 1C plots the transfer characteristics for devices fabricated on the graphene layer, on the MoS_2 layer, and across the interface (channel current, I_{ch}, versus back-gate voltage, V_g). The charge neutrality point of graphene is around 3 V, whereas the threshold voltage of MoS_2 is very negative (around −17 V). The weak nonlinearity of the output characteristics (channel current, I_{ch}, versus channel voltage, V_{ch}, with various V_g), as shown in fig. S4, indicates that the Schottky barrier height at the graphene-MoS_2 interface is relatively low (on the order of 10 meV; see fig. S10), which has also been confirmed by our previous work (*25*) and others (*26*, *27*). Such a weak Schottky junction suggests that the PV effect, if any, would be very weak at the graphene-MoS_2 interface. Figure 1D shows a scanning photocurrent microscopic (SPCM) image of the device with a 633-nm laser excitation (see Materials and Methods for experimental setups), from which it is observed that the strongest photocurrent response is localized at the graphene-MoS_2 junction. The *I*-*V* curves with the 633-nm light shined on the junction, as shown in fig. S5, indicate that there is an electromotive force generated, which rules out any photoconductive or bolometric effect.

Now, let us consider the PTE effect. The photoexcited carriers are first thermalized through either electron-electron scattering or electron-phonon scattering, leading to broader energy distributions of electrons. On the graphene side, because of the linear electronic dispersion and its low dimensionality, the electron-electron scatterings are substantially stronger than the electron-phonon scatterings

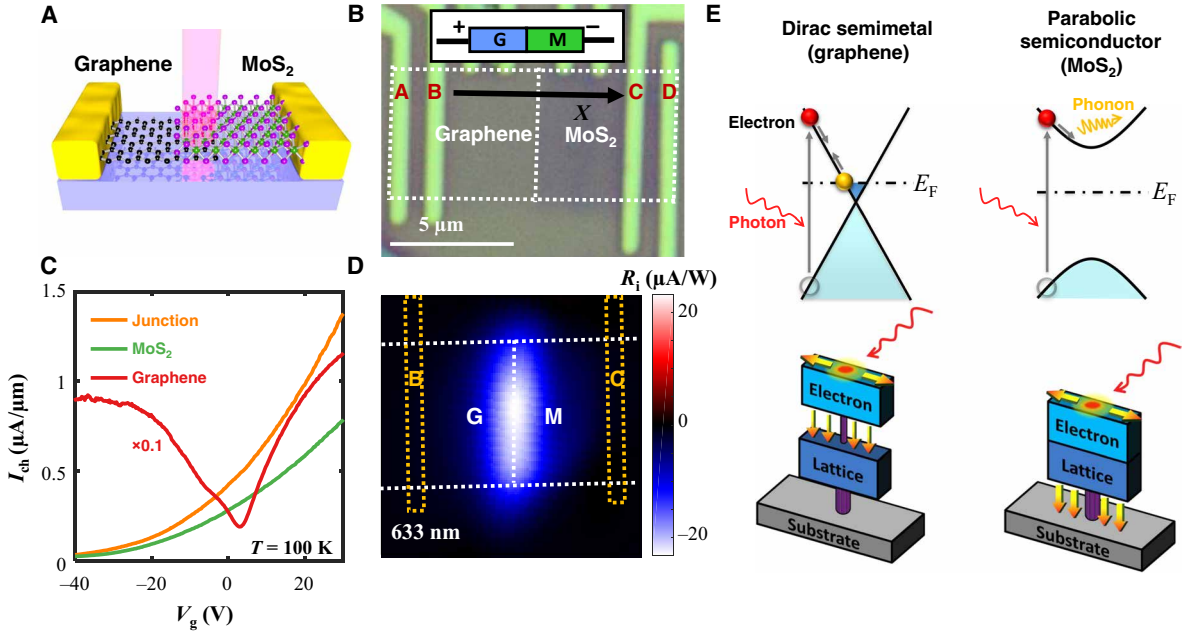

Fig. 1. Graphene-MoS_2 lateral heterojunction photodetector. (**A**) Schematic of the device. (**B**) Microscopic image of the as-fabricated device on a 285-nm SiO_2/Si substrate. Multiple long and short electrodes (Ni/Au) were placed around the lateral junction to probe different regions of the device electrically. The inset diagram indicates the cathode and the anode of the device for the electrical and photocurrent measurements; the axis indicates the direction of the *x* axis for the *X*-V_g mappings and the simulation results. (**C**) Transfer characteristics of the graphene-MoS_2 junction (orange, current applied across electrodes B and C and voltage probed across the short electrodes), MoS_2 (green, across electrodes C and D), and graphene (red, across electrodes A and B), respectively. The channel voltage V_{ch} = 0.1 V. (**D**) Spatial photoresponsivity ($R_i = I_{ph}/P_{in}$, with I_{ph} and P_{in} denoting the photocurrent and the incident light power, respectively) of the device under a 633-nm laser excitation with V_{ch} = 0 V and V_g = 0 V. The dotted lines indicate the channel (in white) and electrodes (in orange) of the device. "G" and "M" are short for graphene and MoS_2, respectively. (**E**) Schematics of the dominating hot-electron cooling processes (top) and the spatial hot-electron thermalization pathways (bottom) of the Dirac semimetallic graphene (left) and the parabolic semiconducting MoS_2 (right). In the bottom panels, the arrows indicate possible heat transfer paths, and the diameters of the purple cylinders connecting the electron, the lattice, and the substrates indicate the strength of thermal couplings.

(including scattering with optical phonons, acoustic phonons, and disorder-assisted supercollisions; see the Supplementary Materials for a detailed discussion) (*33*–*37*). Consequently, electrons in graphene would not reach thermal equilibrium with the lattice before being collected (Fig. 1E, left), given that the cooling length of hot electrons in graphene is typically hundreds of nanometers to micrometers (*5*, *7*, *36*). On the MoS_2 side, however, the electronic dispersion at the band edge is parabolic, in which the electrons and lattices are always in thermal equilibrium because of the much stronger electron-phonon scatterings (Fig. 1E, right, and the Supplementary Materials). Such an asymmetric behavior of heat dissipations on the two sides of the graphene-MoS_2 junction could lead to very asymmetric temperature distributions and unusual photocurrent profiles, which will be discussed later. The increased electron temperature at the graphene-MoS_2 junction (hot side) with respect to the electrodes (cold side) could then be transduced into an electric signal through the Seebeck effect, and the photovoltage is given by $V_{ph} = -(S_{gr} - S_{MoS2})\cdot\Delta T_j^{el}$, with S_{gr} and S_{MoS2} representing the Seebeck coefficients of graphene and MoS_2, respectively, and ΔT_j^{el} denoting the increase of electron temperature at the graphene-MoS_2 junction with respect to the temperature of the unheated substrate. The Seebeck coefficient of graphene follows a nonmonotonic relation with respect to the Fermi level or gate voltage (*5*, *7*, *36*). Given that S_{MoS2} changes very slowly and monotonically with the gate voltage when MoS_2 is heavily doped, the photovoltage induced by the PTE effect should approximately follow the nonmonotonic trend of S_{gr} with gate voltage. Meanwhile, the photovoltage induced by the PV effect should change monotonically with the gate voltage simply because the change of the barrier height at the junction is positively correlated to the difference between the Fermi level shifts of graphene and MoS_2, which could only change monotonically with a global gate voltage.

Gate-dependent SPCM measurements were carried out to confirm that the PTE effect is dominant in the graphene-MoS_2 lateral heterojunction. Figure 2A shows the photocurrent mapping for an 850-nm laser beam sweeping along the linecut across the junction shown in Fig. 1D as the *x* axis while the gate voltage varying for each laser position sweep as the *y* axis. In addition to the main photocurrent peak at the graphene/MoS_2 interface, we also observed two extra peaks at the graphene-metal and the MoS_2-metal junctions. While the photocurrent at the MoS_2-metal junction increases monotonically with the gate voltage, the photocurrent at the graphene-metal junction follows an S-shape curve with the gate voltage (fig. S6). We also observed that the photocurrent at the graphene-MoS_2 junction undergoes a very nonmonotonic change with respect to the gate voltage around the charge neutrality point of graphene. This can be seen more clearly in Fig. 2B, as we stack the gate-dependent photocurrent line profiles on top of each other. The peak photocurrent and the corresponding photovoltage as a function of the gate voltage for four different excitation wavelengths are plotted in the first and second columns of Fig. 2C, where the photovoltages are

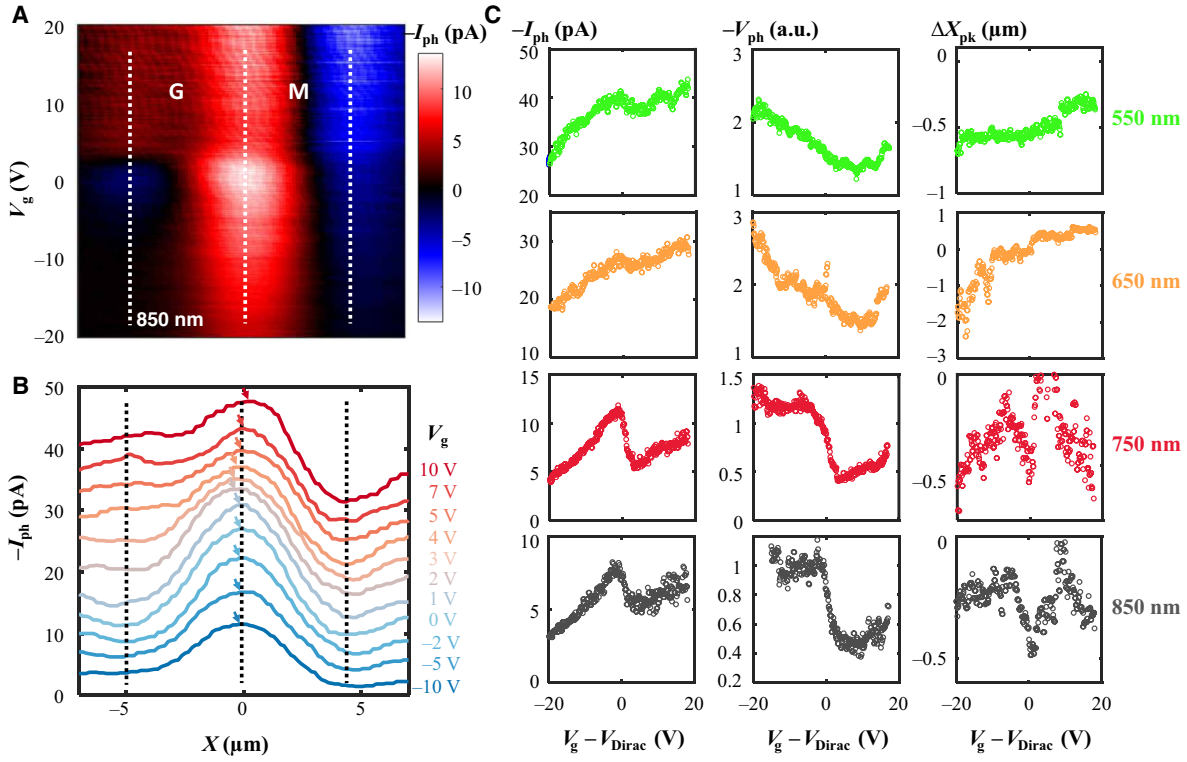

Fig. 2. Gate-dependent SPCM measurements of the device. (**A**) Gate voltage (V_g)–linecut (X) mapping of the photocurrent (I_{ph}) under an 850-nm laser excitation. The three dotted lines indicate (from left to right) the junctions of metal-graphene, graphene-MoS_2, and MoS_2-metal. The magnitude of I_{ph} was flipped to make the photoresponse at the graphene-MoS_2 junction positive. (**B**) Stacked linecuts along the *x* axis of I_{ph} with different V_g. The arrows indicate the peak positions. (**C**) Peak photocurrent I_{ph} (left column), peak photovoltage V_{ph} (middle column), and peak offsets ΔX_{pk} (right column) as a function of the gate voltage with respect to the charge neutrality point of graphene (V_{Dirac}), extracted from the V_g-X mappings with laser excitations of 550 nm (first row), 650 nm (second row), 750 nm (third row), and 850-nm (fourth row). V_{ph} is estimated by $I_{ph}\cdot R_{dark} = I_{ph}\cdot V_{offset}/I_{dark}$, in which the dark resistance R_{dark} is inversely proportional to the dark current I_{dark} averaged throughout the points whenever the laser spot is off the device in the V_g-X mappings, assuming that a constant voltage offset V_{offset} is supplied by the measurement setup. a.u., arbitrary units.

obtained by multiplying the photocurrent value by the resistance of the junction. With shorter excitation wavelengths (550 and 650 nm) or photon energies above the bandgap of MoS_2, both the photocurrent and the photovoltage change monotonically with the gate voltage, whereas an S-shaped relation was observed with longer excitation wavelengths (750 and 850 nm) or photon energies below the bandgap of MoS_2. Given that such an S-shaped photovoltage trend matches well with the trend of the Seebeck coefficient change of graphene as a function of the gate voltage (*5*, *7*), we concluded that the photoresponse mainly originates from the PTE effect, especially at longer wavelengths.

The lateral geometry and the asymmetry of the graphene-MoS_2 junction also make it possible to access different positions around the junction with light excitation. As a result, the spatial patterns due to the vast discrepancy of the thermalization pathways toward the two sides can be revealed. As shown in Fig. 2B and the third column of Fig. 2C, the photocurrent peak position was observed to undergo an unusual shift toward the graphene side by up to 500 nm as the graphene reaches its charge neutrality. This effect could be observed clearly at longer excitation wavelengths (750 and 850 nm). Note that no obvious shifts around graphene's charge neutrality voltage were observed on the graphene-metal or the MoS_2-metal junction (fig. S6). Given that the incident light power is relatively low, the Seebeck coefficients would not be affected by the laser position to the first-order approximation. As a result, the photocurrent profile should follow the profile of the electron temperature change at the lateral junction as we move the laser beam position across the junction.

The photoinduced distribution of electron temperature is governed by the heat transfer equation (*5*, *7*, *40*): $\kappa\nabla^2 T^{el} - g(T^{el} - T_0) + p_{in} = 0$, in which κ and g represent the lateral 2D thermal conductivity and the vertical heat loss, respectively; T^{el} is the electron temperature at a given position; T_0 is the temperature of the substrate; and p_{in} is the input power density, which is provided, in our case, by the incident laser beam. On the MoS_2 side, the total thermal conductivity κ^{tot} and the heat loss into the substrate g^{sub} should be considered as the dominant terms, given that electrons and lattices are considered as a whole, as they are always in thermal equilibrium (Fig. 1E, right). On the graphene side, in contrast, electrons are thermally insulated from the lattice very well, so electron thermal conductivity κ^{el} and the thermal coupling between electrons and lattices $g^{el\text{-}L} = \gamma C^{el}$ with γ and C^{el} representing the electron-lattice cooling rate and electron heat capacity, respectively, govern the heat dissipation and hence determine the electron temperature distribution (Fig. 1E, left). As given in more details in the Supplementary Materials, the typical values of the g and κ ratios are $g^{el\text{-}L}/g^{sub} = 10^{-5}$ to 10^{-1} and $\kappa_{gr}{}^{el}/\kappa_{MoS2}{}^{tot} = 0.01$ to 1.5, which gives rise to much stronger heat dissipations toward the MoS_2 side than toward the graphene side. Figure 3 (A to D) and fig. S14 show the simulated 2D temperature distributions and 1D linecuts across the junction of the device as the laser shines at the graphene, the graphene-MoS_2 junction, and MoS_2 (see the Supplementary Materials for more details about the simulation). It is clearly observed that the peak electron temperature becomes much higher when the laser shines on the graphene side, which matches the aforementioned discussion about the asymmetric heat dissipation pathways. This also explains why the junction temperature ΔT_j^{el} may reach its maximum when the center of the laser spot is away from the geometric junction, toward the graphene direction (Fig. 3F). The distance between the peak position of ΔT_j^{el} and the geometrical junction can be characterized by the cooling length of hot electrons, given by $\xi = (\kappa^{el}/\gamma C^{el})^{1/2}$. ξ becomes

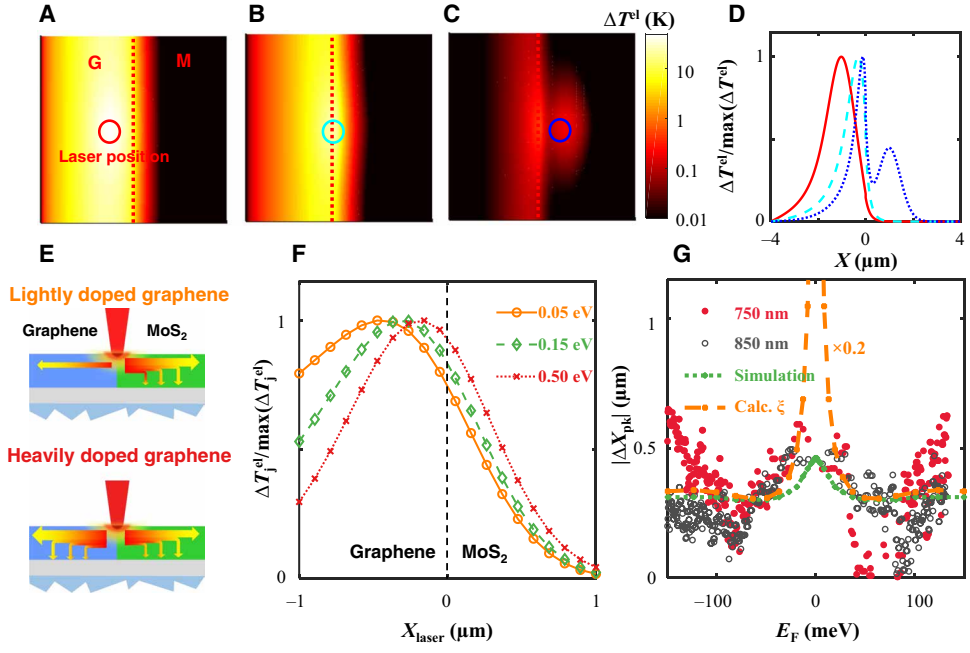

Fig. 3. Theoretical analysis of the thermalization pathways. (**A** to **C**) Simulated distributions of electron temperature increase (ΔT^{el}) as the laser spot is on the graphene side (A), the junction (B), and the MoS_2 side (C). The circles indicate the center positions of the incident laser. (**D**) Linecuts of ΔT^{el} along the *x* axis normalized to the maximum ΔT^{el} as in (A) to (C). (**E**) Schematics of the heat dissipations of photoinduced hot electrons when graphene is lightly doped (with the graphene Fermi level $E_F = 0.05$ eV; top) and heavily doped ($E_F = 0.5$ eV; bottom). (**F**) Normalized electron temperature at the graphene-MoS_2 junction with different E_F. The dashed line indicates the geometric junction. (**G**) Measured magnitudes of peak position offsets ($|\Delta X_{pk}|$) with 750-nm (filled circles) and 850-nm (open circles) laser excitations, as well as the simulated $|\Delta X_{pk}|$ and calculated electron-lattice cooling length on the graphene side (ξ), as a function of E_F.

much bigger as the Fermi level (E_F) of graphene moves toward the charge neutrality point, as shown in figs. S13 and S14. The simulated electron temperature profiles at the junction as the laser spot moves across the junction when graphene is at (lightly doped case; see Fig. 3E, top) and away from (heavily doped case; see Fig. 3E, bottom) the charge neutrality are plotted in Fig. 3F, from which it is observed that the peak of the ΔT_j^{el} profile shifts ~400 nm farther away from the geometrical junction in the lightly doped graphene case than that in the heavily doped graphene case. The trends of the cooling length, the simulated ΔT_j^{el} peak offset with various E_F of graphene, and the peak photocurrent offsets with 750- and 850-nm light excitations are plotted in Fig. 3G, which are in accordance with one another.

Last, we demonstrate the broad spectral range of photoresponses of such a graphene-semiconductor lateral heterojunction promised by the PTE effect. We observed strong photoresponse localized at the graphene-MoS_2 lateral junction from SPCM mappings with a variety of wavelengths ranging from visible to short-wave infrared range (Fig. 1D and fig. S9). In Fig. 4, the spectral photoresponsivity of three different devices is also exhibited. The response at shorter wavelengths (below 700 nm) follows the absorbance of MoS_2, whereas the response at longer wavelengths (above 700 nm) matches better with the absorbance of graphene on a 285-nm SiO_2/Si substrate. This—combined with the different gate-dependent photocurrents, photovoltages, and photocurrent peak positions at shorter wavelengths (550 and 650 nm) and longer wavelengths (750 and 850 nm)—clearly indicates that the photoresponse with the excitation photon energies above and below the MoS_2 bandgap is dominated by the PV or photoconductive effect in MoS_2 and the PTE effect in graphene, respectively. Note that the photoresponsivity reaches its minimum at around 900 nm, which corresponds to the valley of the interference fringes of the substrate. No sign of cutoff was observed in the spectral range (from 500 to 1600 nm) of our measurements. Theoretically, the spectral response of such a structure should be extended to at least 5 μm, limited by the Pauli blocking of graphene (*41*). In addition, the photocurrent scaled linearly with the incident power among all the wavelengths, as shown in fig. S7A. Temperature-dependent measurements reveal a relatively weak nonmonotonic relationship between the photoresponsivity and the temperature

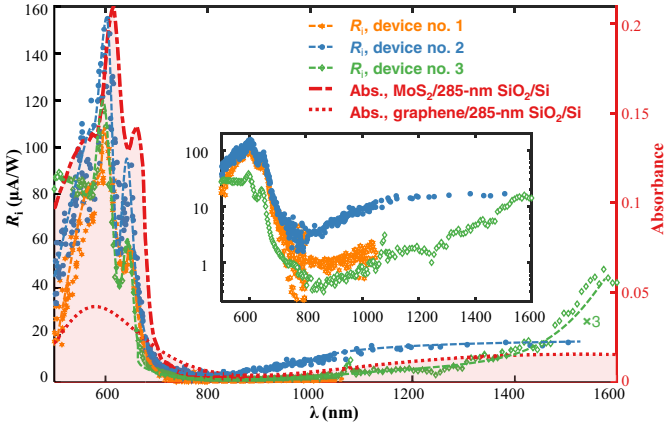

Fig. 4. Spectral photocurrent response of the devices. Left axis: Photocurrent responsivity (R_i) as a function of the wavelength of incident light (λ) of three different devices. Right axis: Calculated absorbance (Abs.) of MoS_2 (red dashed line) and graphene (red dotted line) on a 285-nm SiO_2/Si substrate based on the complex refractive indices from (*42*, *43*). The inset plots the spectral responsivity in log scale.

(fig. S7B), which can be explained by the competition between two hot-carrier cooling mechanisms, that is, acoustic-phonon cooling (dominant at low temperature) and disorder-assisted supercollision cooling (dominant at high temperature) (*36*). Gate-dependent SPCM measurements at different temperatures (fig. S8) reveal that the photocurrent peak position shifts reach maximum at intermediate temperature (50 to 100 K), in accordance with these competing hot-carrier cooling mechanisms as well. According to the ultrafast photocurrent autocorrelation measurement, the intrinsic time constant of the photogeneration process was extracted to be ~14 ps. These observations suggest that the graphene-2D semiconductor lateral heterojunction can be potentially used as a broadband (visible to mid-infrared), ultrafast (~10 ps), and room temperature photodetector.

In summary, we have studied the photoresponse on an asymmetric lateral heterojunction between Dirac semimetal graphene and parabolic semiconductor MoS_2 and have attributed the broadband photoresponse to the PTE effect. A theoretical model was built to describe the asymmetric thermalization pathways of the photogenerated hot carriers, which has successfully explained the spatial feature from experiments. Our study provides a new perspective to study light-matter interactions in low-dimensional systems and paves the way for novel optoelectronic applications with 2D heterostructures. With a rational design of such an in-plane asymmetry, one could possibly study many new phenomena that were either forbidden or requiring more advanced instrumentation in a homogeneous film, including exciton diffusion, dichroic spin-valley photocurrent in 2D semiconductors, electron-electron scattering, and surface plasmon polaritons in graphene.

MATERIALS AND METHODS

Synthesis of graphene/MoS_2 lateral heterojunctions

Graphene flakes were first mechanically exfoliated onto a piranha-cleaned SiO_2/Si substrate by the Scotch tape technique. Before the growth of MoS_2, the exfoliated graphene was annealed at 350°C in Ar [300 sccm (standard cubic centimeters per minute)]/H_2 (100 sccm) for 3 hours to remove the tape residues. The parallel stitching growth of monolayer MoS_2 was enabled by a seeding promoter–diffusion–mediated CVD method (*25*). Perylene-3,4,9,10-tetracarboxylic acid tetrapotassium (PTAS) molecules were used as the seeding promoter. The PTAS was coated onto two additional clean SiO_2/Si pieces, which served as seed reservoirs, from which seeding molecules could selectively diffuse onto the hydrophilic surface of the target substrate for the MoS_2 lateral synthesis. The target substrate (SiO_2/Si wafer with the graphene flakes) was then suspended between those two PTAS-coated SiO_2/Si seed reservoirs. All of these three substrates were faced down and placed on a crucible containing molybdenum oxide (MoO_3; 99.98%) powder precursor. This MoO_3 precursor was put in the middle of a 25.4 millimeter quartz tube as the reaction chamber, and another sulfur powder (99.98%) precursor was placed upstream, 14 cm away from the MoO_3 crucible, in the quartz tube. Before heating, the CVD system was purged using 1000 sccm of Ar (99.999% purity) for 5 min; then, 20 sccm of Ar was introduced into the system as a carrier gas. Next, the temperature of the reaction chamber was increased to 350°C with a rate of 30°C min^{-1} and held at that temperature for 10 min. The temperature was then increased to 610°C with a rate of 30°C min^{-1}. The monolayer MoS_2 parallel stitched on graphene was synthesized at 610°C for 3 min under atmospheric pressure. The temperature of the sulfur source

was kept at ~170°C during growth. Last, the system was cooled down to room temperature quickly using an electric fan. During the cooling process, 1000-sccm Ar flow was maintained in the chamber to remove the reactants, preventing further unintentional reactions.

TEM characterization

The as-grown graphene-MoS_2 heterostructure was transferred onto a TEM grid (Quantifoil, no. 656-200-CU; Ted Pella Inc.) by the poly(methyl methacrylate) (PMMA) method. After transfer onto a TEM grid, the PMMA layer was removed under vacuum annealing at 350°C for half an hour. HRTEM characterization of the heterostructure at the atomic scale was carried out on a JEOL ARM 200CF transmission electron microscope equipped with a cold field-emission electron source and two spherical-aberration correctors operated under an accelerating voltage of 80 kV to reduce radiation damage.

AFM and spectroscopy characterization

The AFM characterization was carried out on a Dimension 3100 instrument, commercially available from Veeco Instruments Inc. PL and Raman spectra were carried out on a HORIBA Jobin-Yvon HR800 system and a WITec alpha 300 confocal Raman microscope. The laser excitation wavelength for the PL and Raman measurements was typically 532.5 nm. The laser power on the sample was about 0.1 mW. A 100× objective was used to focus the laser beam. The spectral parameters were obtained by fitting the peaks using Lorentzian/Gaussian mixed functions as appropriate.

Device fabrication

The graphene-MoS_2 heterostructures were first transferred onto the 285-nm SiO_2/Si substrates with PMMA as the handling supporting layer and diluted hydrofluoric acid (HF) as the oxide etchant to separate the material from the growth substrate. Electron-beam lithography (EBL) and e-beam evaporation followed by a liftoff process were used to deposit 30-nm Ni/20-nm Au stacks as the ohmic contacts to both the graphene and the MoS_2 sides. Another EBL and reactive ion etching with oxygen plasma were used to define the channel area.

Electrical and photocurrent measurements

The transport measurements and spatial photocurrent mappings were carried out with a confocal laser scanning microscopy setup. The chips were wire-bonded onto a chip carrier and mounted in a Janis ST-500 helium optical cryostat equipped with electrical connections, a well-defined microscopic optical path, and a temperature controlling system. The device was kept under high vacuum ($<10^{-5}$ torr) throughout the measurements. Sourcemeters (Agilent B2902a), current preamplifiers (Ithaco DL1211), and data acquisition cards (National Instruments PXI module) were used for the electrical sourcing and probing. Both the transport and the photocurrent measurements were performed at 100 K if not mentioned explicitly in the text. For the scanning photocurrent measurements, a broadband supercontinuum fiber laser (Fianium) was combined with a monochromator to generate the monochromic laser beam with the desired wavelength (tunable from 400 to 1600 nm). A two-axis piezo-controlled scanning mirror was coupled to a microscope objective through two confocal lenses to perform the spatial scanning with the laser beam spot of around 1 μm on the device. The photocurrent and the reflected light intensity were recorded simultaneously to form the scanning photocurrent images and the reflectance images. All the photocurrent results were measured under the short-circuit condition, in which zero voltage bias was applied across the device. The photovoltage corresponds to the open-circuit voltage, in which the current flowing across the junction is set to zero. The absolute location of the photoinduced signal was found by comparing the photocurrent map to the reflection image. The incident laser power was measured at the output of the microscope objective using a calibrated photodetector.

SUPPLEMENTARY MATERIALS

Supplementary material for this article is available at http://advances.sciencemag.org/cgi/content/full/5/6/eaav1493/DC1

Section S1. Additional results on the material characterizations
Section S2. Additional results on the electrical and photocurrent measurements
Section S3. Band diagram of the graphene-MoS_2 lateral heterojunction
Section S4. Electron-phonon coupling strength in graphene and MoS_2
Section S5. Theoretical analysis of the electron temperature distributions
Fig. S1. Atomic force microscope (AFM) image of the graphene-MoS_2 lateral heterojunction.
Fig. S2. HRTEM images of the graphene-MoS_2 lateral heterostructure.
Fig. S3. Raman and PL of the graphene-MoS_2 lateral heterojunction.
Fig. S4. Output characteristics.
Fig. S5. *I-V* characteristics with 633-nm light illumination and various gate voltages.
Fig. S6. Gate-dependent photocurrent response at the graphene-metal and MoS_2-metal junctions.
Fig. S7. Power-dependent and temperature-dependent photocurrent response.
Fig. S8. Photocurrent peak position shift extracted from the V_g-X mappings with 850-nm laser excitation and at various temperatures.
Fig. S9. SPCM mappings of the graphene-MoS_2 junction with different excitation wavelengths.
Fig. S10. Band diagram of the graphene-MoS_2 lateral heterojunction.
Fig. S11. Schematics showing two different hot-electron cooling pathways.
Fig. S12. Extraction of graphene properties.
Fig. S13. Calculated physical parameters for graphene with different Δ values.
Fig. S14. Calculated physical parameters for graphene with different σ_{min} values.
Fig. S15. Simulated electron temperature distributions with different Fermi level of graphene.
References (*44*, *45*)

REFERENCE AND NOTES

1. A. K. Geim, K. S. Novoselov, The rise of graphene. *Nat. Mater.* **6**, 183–191 (2007).
2. J. Chen, M. Badioli, P. Alonso-González, S. Thongrattanasiri, F. Huth, J. Osmond, M. Spasenović, A. Centeno, A. Pesquera, P. Godignon, A. Zurutuza Elorza, N. Camara, F. J. García de Abajo, R. Hillenbrand, F. H. L. Koppens, Optical nano-imaging of gate-tunable graphene plasmons. *Nature* **487**, 77–81 (2012).
3. Z. Fei, A. S. Rodin, G. O. Andreev, W. Bao, A. S. McLeod, M. Wagner, L. M. Zhang, Z. Zhao, M. Thiemens, G. Dominguez, M. M. Fogler, A. H. Castro Neto, C. N. Lau, F. Keilmann, D. N. Basov, Gate-tuning of graphene plasmons revealed by infrared nano-imaging. *Nature* **487**, 82–85 (2012).
4. Z. Fei, A. S. Rodin, W. Gannett, S. Dai, W. Regan, M. Wagner, M. K. Liu, A. S. McLeod, G. Dominguez, M. Thiemens, A. H. Castro Neto, F. Keilmann, A. Zettl, R. Hillenbrand, M. M. Fogler, D. N. Basov, Electronic and plasmonic phenomena at graphene grain boundaries. *Nat. Nanotechnol.* **8**, 821–825 (2013).
5. N. M. Gabor, J. C. W. Song, Q. Ma, N. L. Nair, T. Taychatanapat, K. Watanabe, T. Taniguchi, L. S. Levitov, P. Jarillo-Herrero, Hot carrier–assisted intrinsic photoresponse in graphene. *Science* **334**, 648–652 (2011).
6. M. C. Lemme, F. H. L. Koppens, A. L. Falk, M. S. Rudner, H. Park, L. S. Levitov, C. M. Marcus, Gate-activated photoresponse in a graphene p–n junction. *Nano Lett.* **11**, 4134–4137 (2011).
7. J. C. W. Song, M. S. Rudner, C. M. Marcus, L. S. Levitov, Hot carrier transport and photocurrent response in graphene. *Nano Lett.* **11**, 4688–4692 (2011).
8. D. Sun, G. Aivazian, A. M. Jones, J. S. Ross, W. Yao, D. Cobden, X. Xu, Ultrafast hot-carrier-dominated photocurrent in graphene. *Nat. Nanotechnol.* **7**, 114–118 (2012).
9. C. R. Dean, A. F. Young, I. Meric, C. Lee, L. Wang, S. Sorgenfrei, K. Watanabe, T. Taniguchi, P. Kim, K. L. Shepard, J. Hone, Boron nitride substrates for high-quality graphene electronics. *Nat. Nanotechnol.* **5**, 722–726 (2010).
10. J. Xue, J. Sanchez-Yamagishi, D. Bulmash, P. Jacquod, A. Deshpande, K. Watanabe, T. Taniguchi, P. Jarillo-Herrero, B. J. LeRoy, Scanning tunnelling microscopy and spectroscopy of ultra-flat graphene on hexagonal boron nitride. *Nat. Mater.* **10**, 282–285 (2011).
11. L. A. Ponomarenko, A. K. Geim, A. A. Zhukov, R. Jalil, S. V. Morozov, K. S. Novoselov, I. V. Grigorieva, E. H. Hill, V. V. Cheianov, V. I. Fal'ko, K. Watanabe, T. Taniguchi,

R. V. Gorbachev, Tunable metal–insulator transition in double-layer graphene heterostructures. *Nat. Phys.* **7**, 958–961 (2011).
12. A. K. Geim, I. V. Grigorieva, Van der Waals heterostructures. *Nature* **499**, 419–425 (2013).
13. P. Rivera, J. R. Schaibley, A. M. Jones, J. S. Ross, S. Wu, G. Aivazian, P. Klement, K. Seyler, G. Clark, N. J. Ghimire, J. Yan, D. G. Mandrus, W. Yao, X. Xu, Observation of long-lived interlayer excitons in monolayer $MoSe_2$–WSe_2 heterostructures. *Nat. Commun.* **6**, 6242 (2015).
14. J. R. Schaibley, P. Rivera, H. Yu, K. L. Seyler, J. Yan, D. G. Mandrus, T. Taniguchi, K. Watanabe, W. Yao, X. Xu, Directional interlayer spin-valley transfer in two-dimensional heterostructures. *Nat. Commun.* **7**, 13747 (2016).
15. Q. Ma, T. I. Andersen, N. L. Nair, N. M. Gabor, M. Massicotte, C. H. Lui, A. F. Young, W. Fang, K. Watanabe, T. Taniguchi, J. Kong, N. Gedik, F. H. L. Koppens, P. Jarillo-Herrero, Tuning ultrafast electron thermalization pathways in a van der Waals heterostructure. *Nat. Phys.* **12**, 455–459 (2016).
16. M. Massicotte, P. Schmidt, F. Vialla, K. Watanabe, T. Taniguchi, K. J. Tielrooij, F. H. L. Koppens, Photo-thermionic effect in vertical graphene heterostructures. *Nat. Commun.* **7**, 12174 (2016).
17. W. Xu, W. Liu, J. F. Schmidt, W. Zhao, X. Lu, T. Raab, C. Diederichs, W. Gao, D. V. Seletskiy, Q. Xiong, Correlated fluorescence blinking in two-dimensional semiconductor heterostructures. *Nature* **541**, 62–67 (2016).
18. C.-J. Kim, A. Sánchez-Castillo, Z. Ziegler, Y. Ogawa, C. Noguez, J. Park, Chiral atomically thin films. *Nat. Nanotechnol.* **11**, 520–524 (2016).
19. M. P. Levendorf, C.-J. Kim, L. Brown, P. Y. Huang, R. W. Havener, D. A. Muller, J. Park, Graphene and boron nitride lateral heterostructures for atomically thin circuitry. *Nature* **488**, 627–632 (2012).
20. X. Duan, C. Wang, J. C. Shaw, R. Cheng, Y. Chen, H. Li, X. Wu, Y. Tang, Q. Zhang, A. Pan, J. Jiang, R. Yu, Y. Huang, X. Duan, Lateral epitaxial growth of two-dimensional layered semiconductor heterojunctions. *Nat. Nanotechnol.* **9**, 1024–1030 (2014).
21. C. Huang, S. Wu, A. M. Sanchez, J. J. P. Peters, R. Beanland, J. S. Ross, P. Rivera, W. Yao, D. H. Cobden, X. Xu, Lateral heterojunctions within monolayer $MoSe_2$–WSe_2 semiconductors. *Nat. Mater.* **13**, 1096–1101 (2014).
22. Y. Gong, J. Lin, X. Wang, G. Shi, S. Lei, Z. Lin, X. Zou, G. Ye, R. Vajtai, B. I. Yakobson, H. Terrones, M. Terrones, B. K. Tay, J. Lou, S. T. Pantelides, Z. Liu, W. Zhou, P. M. Ajayan, Vertical and in-plane heterostructures from WS_2/MoS_2 monolayers. *Nat. Mater.* **13**, 1135–1142 (2014).
23. M.-Y. Li, Y. Shi, C.-C. Cheng, L.-S. Lu, Y.-C. Lin, H.-L. Tang, M.-L. Tsai, C.-W. Chu, K.-H. Wei, J.-H. He, W.-H. Chang, K. Suenaga, L.-J. Li, Epitaxial growth of a monolayer WSe_2-MoS_2 lateral p-n junction with an atomically sharp interface. *Science* **349**, 524–528 (2015).
24. X.-Q. Zhang, C.-H. Lin, Y.-W. Tseng, K.-H. Huang, Y.-H. Lee, Synthesis of lateral heterostructures of semiconducting atomic layers. *Nano Lett.* **15**, 410–415 (2015).
25. X. Ling, Y. Lin, Q. Ma, Z. Wang, Y. Song, L. Yu, S. Huang, W. Fang, X. Zhang, A. L. Hsu, Y. Bie, Y.-H. Lee, Y. Zhu, L. Wu, J. Li, P. Jarillo-Herrero, M. Dresselhaus, T. Palacios, J. Kong, Parallel stitching of 2D materials. *Adv. Mater.* **28**, 2322–2329 (2016).
26. M. Zhao, Y. Ye, Y. Han, Y. Xia, H. Zhu, S. Wang, Y. Wang, D. A. Muller, X. Zhang, Large-scale chemical assembly of atomically thin transistors and circuits. *Nat. Nanotechnol.* **11**, 954–959 (2016).
27. M. H. D. Guimarães, H. Gao, Y. Han, K. Kang, S. Xie, C.-J. Kim, D. A. Muller, D. C. Ralph, J. Park, Atomically thin ohmic edge contacts between two-dimensional materials. *ACS Nano* **10**, 6392–6399 (2016).
28. Z. Zhang, P. Chen, X. Duan, K. Zang, J. Luo, X. Duan, Robust epitaxial growth of two-dimensional heterostructures, multiheterostructures, and superlattices. *Science* **357**, 788–792 (2017).
29. S. Xie, L. Tu, Y. Han, L. Huang, K. Kang, K. U. Lao, P. Poddar, C. Park, D. A. Muller, R. A. DiStasio Jr., J. Park, Coherent, atomically thin transition-metal dichalcogenide superlattices with engineered strain. *Science* **359**, 1131–1136 (2018).
30. X. Xu, N. M. Gabor, J. S. Alden, A. M. van der Zande, P. L. McEuen, Photo-thermoelectric effect at a graphene interface junction. *Nano Lett.* **10**, 562–566 (2010).
31. K. J. Tielrooij, J. C. W. Song, S. A. Jensen, A. Centeno, A. Pesquera, A. Zurutuza Elorza, M. Bonn, L. S. Levitov, F. H. L. Koppens, Photoexcitation cascade and multiple hot-carrier generation in graphene. *Nat. Phys.* **9**, 248–252 (2013).
32. K. J. Tielrooij, L. Piatkowski, M. Massicotte, A. Woessner, Q. Ma, Y. Lee, K. S. Myhro, C. N. Lau, P. Jarillo-Herrero, N. F. van Hulst, F. H. L. Koppens, Generation of photovoltage in graphene on a femtosecond timescale through efficient carrier heating. *Nat. Nanotechnol.* **10**, 437–443 (2015).
33. R. Bistritzer, A. H. MacDonald, Electronic cooling in graphene. *Phys. Rev. Lett.* **102**, 206410 (2009).
34. J. C. W. Song, M. Y. Reizer, L. S. Levitov, Disorder-assisted electron-phonon scattering and cooling pathways in graphene. *Phys. Rev. Lett.* **109**, 106602 (2012).
35. M. W. Graham, S.-F. Shi, D. C. Ralph, J. Park, P. L. McEuen, Photocurrent measurements of supercollision cooling in graphene. *Nat. Phys.* **9**, 103–108 (2013).
36. Q. Ma, N. M. Gabor, T. I. Andersen, N. L. Nair, K. Watanabe, T. Taniguchi, P. Jarillo-Herrero, Competing channels for hot-electron cooling in graphene. *Phys. Rev. Lett.* **112**, 247401 (2014).
37. J. C. W. Song, L. S. Levitov, Energy flows in graphene: Hot carrier dynamics and cooling. *J. Phys. Condens. Matter* **27**, 164201 (2015).
38. X. Ling, Y.-H. Lee, Y. Lin, W. Fang, L. Yu, M. S. Dresselhaus, J. Kong, Role of the seeding promoter in MoS_2 growth by chemical vapor deposition. *Nano Lett.* **14**, 464–472 (2014).
39. H. Yu, A. Kutana, B. I. Yakobson, Carrier delocalization in two-dimensional coplanar p–n junctions of graphene and metal dichalcogenides. *Nano Lett.* **16**, 5032–5036 (2016).
40. E. Pop, D. A. Mann, K. E. Goodson, H. Dai, Electrical and thermal transport in metallic single-wall carbon nanotubes on insulating substrates. *J. Appl. Phys.* **101**, 093710 (2007).
41. P. Avouris, M. Freitag, Graphene photonics, plasmonics, and optoelectronics. *IEEE J. Sel. Top. Quantum Electron.* **20**, 72–83 (2014).
42. K. F. Mak, M. Y. Sfeir, Y. Wu, C. H. Lui, J. A. Misewich, T. F. Heinz, Measurement of the optical conductivity of graphene. *Phys. Rev. Lett.* **101**, 196405 (2008).
43. Y. Li, A. Chernikov, X. Zhang, A. Rigosi, H. M. Hill, A. M. van der Zande, D. A. Chenet, E.-M. Shih, J. Hone, T. F. Heinz, Measurement of the optical dielectric function of monolayer transition-metal dichalcogenides: MoS_2, $MoSe_2$, WS_2, and WSe_2. *Phys. Rev. B* **90**, 205422 (2014).
44. K. Kaasbjerg, K. S. Bhargavi, S. S. Kubakaddi, Hot-electron cooling by acoustic and optical phonons in monolayers of MoS_2 and other transition-metal dichalcogenides. *Phys. Rev. B* **90**, 165436 (2014).
45. R. Yan, J. R. Simpson, S. Bertolazzi, J. Brivio, M. Watson, X. Wu, A. Kis, T. Luo, A. R. Hight Walker, H. G. Xing, Thermal conductivity of monolayer molybdenum disulfide obtained from temperature-dependent Raman spectroscopy. *ACS Nano* **8**, 986–993 (2014).

Acknowledgments
Funding: This material is based upon work sponsored in part by the U.S. Army Research Office through the Institute for Soldier Nanotechnologies, under Cooperative Agreement number W911NF-18-2-0048, AFOSR FATE MURI, grant no. FA9550-15-1-0514, and the STC Center for Integrated Quantum Materials, NSF grant no. DMR 1231319. P.-C.S. and J.K. acknowledge the support from the NSF Center for Energy Efficient Electronics Science (E3S), under NSF grant no. ECCS-0939514. Q.M., Y.B., and P.J.-H. were partly supported through AFOSR grant FA9550-16-1-0382 and the Gordon and Betty Moore Foundation's EPiQS Initiative through grant GBMF4541 (to P.J.-H.). X.L. acknowledges the support from Boston University and the membership of Photonics Center of Boston University. X.Z., N.M., and J.K. acknowledge the NSF grant NSF DMR-1507806 and NSF 2DARE (grant no. EFRI-1542815) for financial support. X.J., J.K., Q.M., Y.B., and P.J.-H. acknowledge the partial support by the Center for Excitonics, an Energy Frontier Research Center funded by the Basic Energy Sciences program of the U.S. Department of Energy Office of Science (award no. DE-SC0001088). B.I., E.E., and N.G. acknowledge the support from the Department of Energy, under award no. BES DE-SC0012509. This work was performed in part at the Microsystems Technology Laboratories (MTL) at MIT and the Harvard University Center for Nanoscale Systems (CNS), a member of the National Nanotechnology Coordinated Infrastructure Network (NNCI), which is supported by the NSF under NSF ECCS award no. 1541959. **Author contributions:** Y.L., Q.M., X.L., J.K., and T.P. conceived the experiment. P.-C.S., X.L., and X.J. contributed to the material synthesis supervised by J.K.. Y.L., B.H., and Y.B. conducted mechanical exfoliation. Y.L. fabricated the devices. Y.L., Q.M., and Y.B. carried out the transport and photocurrent measurements supervised by T.P. and P.J.-H.. B.I. and E.E. conducted additional time-resolved photocurrent measurements supervised by N.G. Y.L. and A.L. performed the simulation. Y.L., X.L., P.-C.S., and S.H. conducted TEM, AFM, and Raman/PL characterizations. Y.L., Q.M., and B.H. analyzed the data. Y.B., X.Z., N.M., S.H., M.D., Y.Z., and J.Y. contributed to discussions and interpretations of the data. Y.L., Q.M., P.-C.S., X.L., J.K., and T.P. cowrote the paper with input from all the authors. **Competing interests:** The authors declare that they have no competing interests. **Data and materials availability:** All data needed to evaluate the conclusions in the paper are present in the paper and/or the Supplementary Materials. Additional data related to this paper may be requested from the authors.

Submitted 18 August 2018
Accepted 9 May 2019
Published 14 June 2019
10.1126/sciadv.aav1493

Citation: Y. Lin, Q. Ma, P.-C. Shen, B. Ilyas, Y. Bie, A. Liao, E. Ergeçen, B. Han, N. Mao, X. Zhang, X. Ji, Y. Zhang, J. Yin, S. Huang, M. Dresselhaus, N. Gedik, P. Jarillo-Herrero, X. Ling, J. Kong, T. Palacios, Asymmetric hot-carrier thermalization and broadband photoresponse in graphene-2D semiconductor lateral heterojunctions. *Sci. Adv.* **5**, eaav1493 (2019).

Science Advances

Asymmetric hot-carrier thermalization and broadband photoresponse in graphene-2D semiconductor lateral heterojunctions

Yuxuan Lin, Qiong Ma, Pin-Chun Shen, Batyr Ilyas, Yaqing Bie, Albert Liao, Emre Ergeçen, Bingnan Han, Nannan Mao, Xu Zhang, Xiang Ji, Yuhao Zhang, Jihao Yin, Shengxi Huang, Mildred Dresselhaus, Nuh Gedik, Pablo Jarillo-Herrero, Xi Ling, Jing Kong and Tomás Palacios

Sci Adv **5** (6), eaav1493.
DOI: 10.1126/sciadv.aav1493